Quantitative analysis of grazing incidence small-angle x-ray scattering: Pd/MgO(001) growth

C. Revenant,[1] F. Leroy,[1] R. Lazzari,[1,2] G. Renaud,[1] and C. R. Henry[3]
[1]*Département de Recherche Fondamentale sur la Matière Condensée/SP2M/NRS, CEA Grenoble, 17 Avenue des Martyrs, F-38054 Grenoble Cedex 9, France*
[2]*Groupe de Physique des Solides, CNRS and Universités Paris 6-7 UMR 7588, 2 Place Jussieu, F-75251 Paris Cedex 05, France*
[3]*Centre de Recherche sur les Mécanismes de la Croissance Cristalline, Campus de Luminy, Case 913, F-13288 Marseille Cedex 09, France*
(Received 13 June 2003; revised manuscript received 22 September 2003; published 27 January 2004)

The present paper focuses on the analysis of grazing incidence small-angle x-ray scattering (GISAXS) of islands on a substrate. Getting accurate morphological parameters relevant for the elaboration process, i.e., growth curves, island equilibrium shape, and interfacial energy, implies a quantitative data analysis. The emphasis is put on the island form factor, i.e., the Fourier transform of the island shape. It is shown that the island shape and size can be obtained through the island symmetry, the presence of island facets, the asymptotic behavior at high momentum transfer for large polydispersity, and the zeros or minima of the intensity for small polydispersity. The specificity brought by the grazing incidence scattering geometry is highlighted by a careful comparison between the Born approximation and the more accurate distorted wave Born approximation. The interplay between the form factor and the interference function is all the more important in the total scattering intensity when incoherent diffuse scattering comes into play at small momentum transfer for disordered systems. Getting rid of these interpretation difficulties requires accurate measurements of the scattered intensity far in the reciprocal space. This analysis methodology is illustrated through recently acquired GISAXS patterns during the *in situ* molecular beam epitaxy of Pd nanoislands on MgO(001) single crystals for different thicknesses and temperatures. The morphological parameters obtained agree very well with subsequent transmission electron microscopy-results. Finally, GISAXS diffuse scattering has been shown, originating from the growth-coalescence process and from the size dependence of the island capture area.

DOI: 10.1103/PhysRevB.69.035411 PACS number(s): 68.37.−d, 61.10.Eq, 61.46.+w, 07.05.Tp

I. INTRODUCTION

The past few decades have been marked by the study of materials on a nanometric scale, such as deposited layers, multilayers, and more recently clusters, aggregates, and nanosized materials. These nanomaterials often have interesting macroscopic properties, electronic, photonic, magnetic, or catalytic, which are intimately linked to their internal structure and their morphology. In this context, many techniques have been developed to characterize their structure and morphology. The most widely used are imaging techniques such as transmission electron microscopy (TEM) and near field microscopies like scanning tunneling microscopy (STM) and atomic force microscopy. If these techniques most often provide the required information, it may be advantageous, in some cases, to complement these real space imaging techniques with x-ray measurements. Indeed, x rays present several advantages. First, an averaged statistics over the whole sample is performed, thus sampling in the same way as for the macroscopic properties of interest. In addition, *in situ* and real time experiments can be performed in various environments (from ultrahigh vacuum to high pressure gases). Finally, because of the variable probed depth as a function of the incident angle, x rays can characterize surface morphology as well as the roughness of buried interfaces. Thus, the grazing incidence small-angle x-ray scattering (GISAXS) technique has emerged in the last decade as a powerful tool to analyze the morphology and distribution of either islands on a substrate or buried particles.[1–3] The GISAXS ability to characterize granular multilayered systems[4] and implanted systems,[5] as well as semiconductor quantum dots obtained by molecular beam epitaxy (MBE) or liquid phase epitaxy, is now well established.[6,7] Recent developments consisted in GISAXS measurements performed in ultrahigh vacuum (UHV), *in situ*, during MBE, and with no scattering element between the undulator synchrotron x-ray source and the detector, thus yielding a very high sensitivity and background-free data.[8] This provides data extending far away in reciprocal space with intensity variation over several orders of magnitude, thus evidencing many GISAXS features that could not be revealed in previous measurements. For this reason, precise quantitative analysis can be performed, as will be shown in this paper. In particular, the GISAXS technique has been used to characterize, *in situ*, and in UHV, the growth of metal/oxide interfaces, like Pd islands on MgO(001),[9,10] and the self-organized growth of Co clusters on the herringbone reconstruction of the Au(111) surface.[11]

In order to get accurate morphological characteristics of the islands, it is extremely important to carry out a precise quantitative GISAXS analysis. The purpose of this article is to show how a two-dimensional (2D) GISAXS pattern can be precisely analyzed to deduce the average interisland distance, island shape, size, and size distributions. First, the general expression for small-angle scattering by islands is recalled within the Born approximation (BA). It is made of a

coherent term, plus an incoherent scattering term due to the presence of the size distribution and possible correlation between the islands. The coherent term is the product of the square modulus of the mean island form factor and of an interference function, which are, respectively, the Fourier transform (FT) of the island shape and that of the island-island correlation function. Next, the two usual approximations to evaluate the incoherent scattering are introduced: the decoupling approximation (DA), assuming no island correlations, and the local monodisperse approximation (LMA), assuming full correlation between island sizes at a scale corresponding to the coherence length of the x-ray beam. Since GISAXS is performed under grazing incidence and emergence conditions, the evaluation of the form factor in the BA is inadequate. Thus the intensity expression obtained within the distorted wave Born approximation (DWBA) is recalled. This latter involves the coherent interference between four scattering patterns, in a way that is very sensitive to the exact value of the incident angle. This additional complexity is then discussed. The form factors are evaluated and compared for several simple island shapes: cylinder, totally or partially emerging sphere, and complete or truncated fourfold pyramid. Information on the island shape can be obtained from the island symmetry probed by a sample rotation around its surface normal and from possible island facets shown by scattering rods. Furthermore, inspection of the intensity zeros or minima may be of great help to determine the average size, at least when all islands are nearly identical. Nevertheless, the islands are in general polydisperse and present a size distribution, in which case the above criteria are not sufficient. Then we show that the asymptotic behavior may allow precise determination of the average shape. In concentrated systems, the GISAXS pattern is strongly affected by the interference function, which thus has to be properly evaluated for quantitative analysis. The usual theoretical or phenomenological pair correlation functions are shown to yield inadequate interference functions at very small angles.[12] Hence, for the present Pd/MgO(001) case, the island-island pair correlation function (and then the interference function) has been directly evaluated from TEM plane views of the deposits. We also show that the interisland distance cannot be determined directly from the total scattering intensity and can only result from a complete quantitative analysis. Finally, we show some incoherent diffuse scattering located at small momentum transfer, which cannot be accounted for by the usual DA or LMA. It is shown to originate from correlations between island sizes and separations, and is evaluated from TEM plane views.

This GISAXS analysis procedure is finally applied to 2D GISAXS measurements performed on four Pd/MgO(001) deposits formed at different temperatures (550, 650, and 740 K) and for different thickness (0.1, 0.9, 1.0, and 3.0 nm).

II. GISAXS THEORY

A. Grazing incidence geometry

The grazing incidence geometry is shown in Fig. 1. The incident x-ray beam is characterized by the wave vector $\mathbf{k}_i = (\mathbf{k}_{i\parallel}, \mathbf{k}_{i\perp})$ defined by the in-plane and out-of-plane angles (θ_i, α_i). In a similar way, the scattered beam of wave vector $\mathbf{k}_f$ is defined by the in-plane and out-of-plane angles (θ_f, α_f). The momentum transfer is defined as $\mathbf{q} = \mathbf{k}_f - \mathbf{k}_i$ and can be expressed as

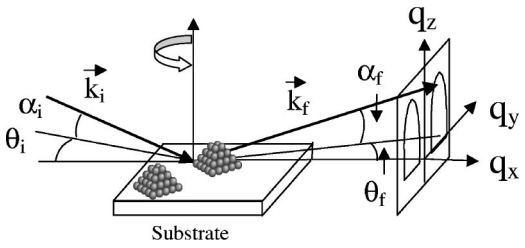

FIG. 1. Scattering geometry of GISAXS. The incident x-ray beam (wave vector $\mathbf{k}_i$) impinges on the surface at a grazing angle α_i with respect to the surface and with an in-plane angle θ_i with respect to a chosen axis linked to the sample and parallel to the sample surface. The transmitted and reflected beams are not represented here. The sample can be rotated around its surface normal. The scattered intensity is recorded on a plane as a function of the exit angle α_f with respect to the surface plane and of the in-plane angle θ_f. The momentum transfer is denoted $\mathbf{q} = (q_x, q_y, q_z)$.

$$\mathbf{q} = \frac{2\pi}{\lambda} \begin{pmatrix} \cos(\alpha_f)\cos(\theta_f) - \cos(\alpha_i)\cos(\theta_i) \\ \cos(\alpha_f)\sin(\theta_f) + \cos(\alpha_i)\sin(\theta_i) \\ \sin(\alpha_f) + \sin(\alpha_i) \end{pmatrix}, \qquad (1)$$

where λ is the x-ray wavelength.

B. Scattered intensity

1. Small-angle scattering by islands on a substrate

First, let us consider the intensity scattered by an assembly of islands whose positions and shapes can be statistically defined. The scattered intensity $I(\mathbf{q})$ is the sum of a coherent term and an incoherent one:[13,14]

$$I(\mathbf{q}) = S(\mathbf{q}_\parallel) \times |\overline{F(\mathbf{q})}|^2 + \sum_m \Phi_m(\mathbf{q}) \times e^{-i\mathbf{q}\cdot\mathbf{r}_m}, \qquad (2)$$

where $S(\mathbf{q}_\parallel)$ is the 2D interference function of the island assembly.[12] It is the FT of the island position autocorrelation function. The overbar on $F(\mathbf{q})$ denotes the spatial averaging of $F(\mathbf{q})$. In Eq. (2), $F(\mathbf{q})$, the island form factor, is the amplitude scattered by an island of volume V and electronic density ρ irradiated by the incident beam.[15] In the BA, it is given by the FT of the island electronic density:

$$F(\mathbf{q}) = \int_V \rho(\mathbf{r}) e^{-i\mathbf{q}\cdot\mathbf{r}} dV. \qquad (3)$$

The $\Phi_m(\mathbf{q})$ coefficient in Eq. (2), describing the correlations between island sizes, is given by

$$\Phi_m(\mathbf{q}) = \overline{[F_n(\mathbf{q}) - \overline{F(\mathbf{q})}][F_{n+m}(\mathbf{q}) - \overline{F(\mathbf{q})}]^*}^n, \qquad (4)$$

where the n superscript denotes the average over all islands n and $F_n(\mathbf{q})$ is the form factor of the island n. The function $\Phi_m(\mathbf{q})$ is a measure of the correlation between the scattering amplitude of two islands separated by a vector $\mathbf{r}_m$. The sum-

mation over $\Phi_m(\mathbf{q})$ in Eq. (2) yields the incoherent diffuse scattering arising from such correlations.[16] Two approximations are commonly used to evaluate this incoherent scattering.

a. DA. For systems with small polydispersities, the DA is appropriate.[13,15] It supposes that the nature of the scatterers and their positions are not correlated, so that the partial pair correlation functions depend only on the relative positions of the scatterers, i.e., $\Phi_m(\mathbf{q})=0$ for $m\neq 0$. Only the $m=0$ term remains:

$$\Phi_0(\mathbf{q})=\overline{|F(\mathbf{q})|^2}-|\overline{F(\mathbf{q})}|^2. \tag{5}$$

b. LMA. For polydispersed systems, the LMA is commonly used. Neighboring islands are assumed to have the same shape and size, over the coherent area of the x-ray beam.[17,18] The intensity is thus the incoherent summation of that of monodisperse subsystems weighted by the size distribution. The intensity originating from one monodisperse domain i is

$$I_i(\mathbf{q})=S_i(\mathbf{q})\times|F_i(\mathbf{q})|^2. \tag{6}$$

The incoherent sum of the intensity over all the domains is then

$$I(\mathbf{q})=\sum_i I_i(\mathbf{q})\approx S(\mathbf{q})\times\overline{|F_i(\mathbf{q})|^2}, \tag{7}$$

assuming that the same interference function holds for all the domains. Note that the DA and LMA are equivalent at large $\mathbf{q}$, as the $\Phi_0(\mathbf{q})$ term then decreases toward zero.

2. Form factor within the DWBA

GISAXS is generally performed with the incident angle α_i near the critical angle for total external reflection α_c in order to minimize the bulk scattering and to increase surface sensitivity.[19] At these low angles, the surface acts as a mirror and multiple scattering effects come into play leading to the inadequacy of the BA. Briefly, the DWBA is an extension of single scattering (BA) through a perturbation treatment of the island-induced roughness.[20,21] Hence, a very different expression is obtained,[22] in which the form factor $F(\mathbf{q})$ is replaced by the coherent sum of four terms, which represent different scattering events involving or not a reflection of either the incident or final beam on the substrate surface. Each term comprises the island form factor, evaluated at different values $\pm q_z=\pm(k_z^f-k_z^i)$ and $\pm p_z=\pm(k_z^f+k_z^i)$, and weighted by the Fresnel reflection coefficients $R(\alpha_i)$ and $R(\alpha_f)$ of the substrate:

$$F(\mathbf{q}_\parallel,k_i^z,k_f^z)=F(\mathbf{q}_\parallel,q_z)+R(\alpha_f)F(\mathbf{q}_\parallel,-p_z)+R(\alpha_i)F(\mathbf{q}_\parallel,p_z)+R(\alpha_i)R(\alpha_f)F(\mathbf{q}_\parallel,-q_z). \tag{8}$$

For substrates with an uncorrelated roughness, the Fresnel reflection coefficients are modified by a decreasing exponential term depending on the rms roughness σ, the z component of the wave vector in vacuum and that of the wave vector in the substrate.[23] In this GISAXS study, the reference system for the DWBA is the bare substrate, although it might be useful to take into account the surface roughness induced by the islands in the form of a Debye-Waller factor for the Fresnel reflection coefficients.[22]

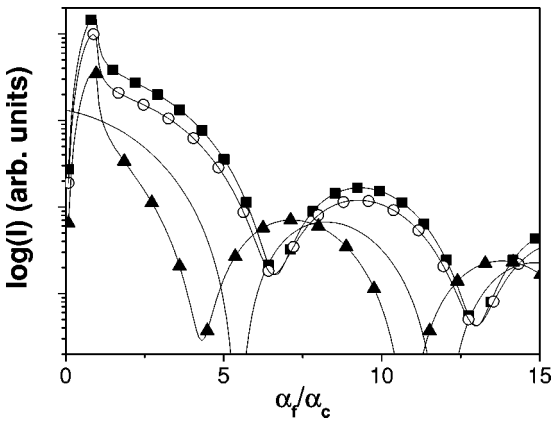

FIG. 2. Out-of-plane GISAXS intensity (logarithmic basis) for a cylinder ($H=5$ nm) as a function of α_f/α_c and at $\theta_f=0$. Filled squares, DWBA for $\alpha_i=\alpha_c$; triangles, DWBA for $\alpha_i=2\alpha_c$; open circles, DWBA for $\alpha_i=\alpha_c/2$; continuous line, BA.

The form factor within the BA is given by this relation with $R(\alpha_i)=R(\alpha_f)=0$. Hence, the BA is valid only when the Fresnel reflectivities are negligible, which is the case when α_i and α_f are much larger than α_c.

The scattered intensities evaluated within the BA or the DWBA may differ widely. As an example, both intensities are compared along the perpendicular direction in Fig. 2. Due to the multiple scattering effects, the intensity displays a sharp increase for $\alpha_f\approx\alpha_c$. Moreover, the BA intensity has deep minima as opposed to much slighter minima obtained within the DWBA. For $\alpha_i=\alpha_c$ or $\alpha_c/2$ ($2\alpha_c$), the minima obtained within the DWBA are shifted toward larger (smaller) exit angles with respect to those obtained within the BA. Figure 3 represents the square modulus of the four terms of Eq. (8) versus α_f/α_c for $\alpha_i=\alpha_c$, $2\alpha_c$, and $\alpha_c/2$. For $\alpha_i=\alpha_c$ and $\alpha_c/2$, the first term $F(\mathbf{q}_\parallel,q_z)$ and the third one $R(\alpha_i)F(\mathbf{q}_\parallel,p_z)$ have a similar magnitude over the whole range of exit angles. The addition of this third term attenuates the minima and shifts them. The second and fourth terms are negligible, except for $\alpha_f\leqslant\alpha_c$. In short, because of a complex interference between the four terms in Eq. (8) whose amplitudes and phases depend on the incident and exit angles,[12] the BA is unable to describe the scattered intensity when α_i is close to α_c. On the contrary, if $\alpha_i\gg\alpha_c$ and $\alpha_f\gg\alpha_c$, the BA is a good approximation. At powerful synchrotron facilities, it could be thought relevant to carry out GISAXS at $\alpha_i\geqslant 2\alpha_c$, as some quick analysis could be done in the BA. However, in this case, some information is lost for small q_z values [$q_z^{\min}=(2\pi/\lambda)\times\sin(\alpha_i)$ from Eq. (1)].

For simplicity, the following discussion is restricted to the island form factor as a simple square modulus of the FT, all the more since only the scattered intensity parallel to the surface is concerned. Nevertheless, it has to be stressed that

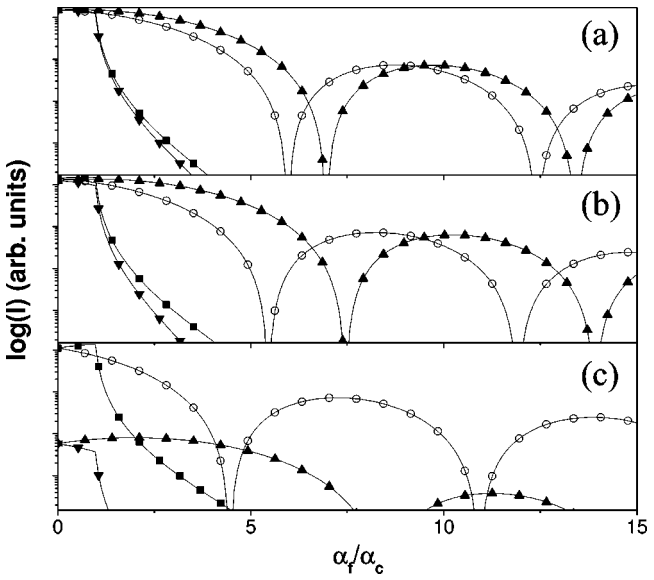

FIG. 3. Square modulus (logarithmic basis) of the four terms of Eq. (8) for a cylinder ($H=5$ nm) as a function of α_f/α_c and at $\theta_f=0$ for (a) $\alpha_i=\alpha_c/2$, (b) $\alpha_i=\alpha_c$, and (c) $\alpha_i=2\alpha_c$. Open circles, $F(\mathbf{q}_\parallel,q_z)$; up triangles, $R(\alpha_i)F(\mathbf{q}_\parallel,p_z)$; filled squares, $R(\alpha_f)F(\mathbf{q}_\parallel,-p_z)$; down triangles, $R(\alpha_i)R(\alpha_f)F(\mathbf{q}_\parallel,-q_z)$.

all the simulations performed on the experimental results (acquired for α_i close to α_c) are performed within the DWBA.

C. Form factor

1. Introduction

The most interesting specificity of GISAXS is to probe the island morphology, i.e., shape and size, which can be derived in principle from the form factor. However, the scattered intensity is the product of this form factor by an interference function as illustrated in Fig. 4. In the case of concentrated systems, these two terms are strongly correlated at small q_y values. Nevertheless, in disordered systems, the interference function tends to 1 as the momentum transfer increases, and the GISAXS intensity is then entirely determined by the form factor. Hence, in order to discriminate between different shapes and accurately determine the island size and size distribution, the intensity must be measured (i) far from the origin in reciprocal space and (ii) over several orders of magnitude. This requires a background as low as possible as the form factor decreases rapidly with increasing q values.

Several methods can be used to determine simple island shapes. First, the symmetry of the GISAXS intensity as the sample is rotated around its surface normal allows one to determine the symmetry of the island shape. Second, scattering rods, if present, indicate island facets. Third, the island shape can be deduced by analyzing the asymptotic behavior of the intensity in the case of large polydispersity (see Sec. II C 3 c below).

We show also that, for small polydispersity, simple features of the intensity, such as the positions of zeros or minima, are related to the island size. Actually, we restrict

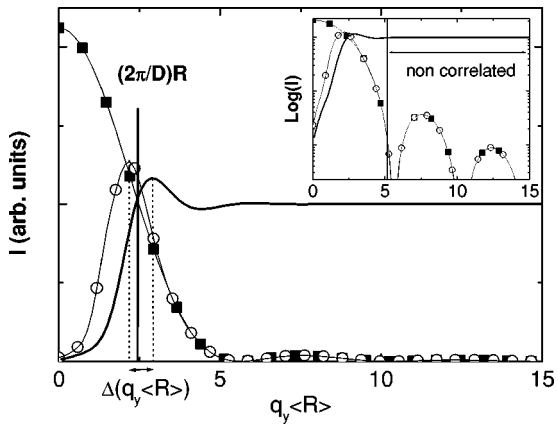

FIG. 4. Open circles, GISAXS intensity calculated within the BA as a function of the parallel momentum transfer $q_y\langle R\rangle$ and at $\alpha_f=0$ for cylindrical islands on a substrate in a disordered state. Filled squares, form factor of a cylinder. Continuous line, interference function with a distance between islands of $D=2.4\times\langle R\rangle$. The difference between the maximum of the interference function and that of the GISAXS intensity is $\Delta(q_y\langle R\rangle)$. The inset shows the same evolution with the y axis on a logarithmic scale.

ourselves to the parallel case (lateral size) where these relations are more systematic.

2. Form factors of simple geometrical shapes

The analytic expressions of the form factors for simple island shapes are given elsewhere.[12] For anisotropic islands, the form factor depends on the orientation of the island with respect to the x-ray beam. When the frame linked to the island is not aligned with the axis of the incident beam, the analytic expressions of the form factor can be applied after rotating the momentum transfer according to

$$\begin{pmatrix} \cos(\zeta) & -\sin(\zeta) & 0 \\ \sin(\zeta) & \cos(\zeta) & 0 \\ 0 & 0 & 1 \end{pmatrix} \begin{pmatrix} q_x \\ q_y \\ q_z \end{pmatrix}, \tag{9}$$

where ζ is the angle between the direct beam and the island edge. For a pyramid with square base, we distinguish two extreme cases: the x-ray beam aligned along a face or along an edge.

Figure 5 shows 2D maps of $|F(\mathbf{q})|^2$ in the (q_y,q_z) space calculated within the DWBA for various island shapes and orientations at $\theta_i=0$ and $\alpha_i=\alpha_c$. On these five maps, the intensity presents a maximum along the perpendicular direction at $\alpha_f=\alpha_c$ due to the interference effects between the four scattered beams on the surface. For a cylinder, the pattern is composed of well separated lobes along both parallel and perpendicular directions [cf. Fig. 5(a)]. For a complete sphere, one main zero-order lobe is present, with a first-order arc-shaped lobe [cf. Fig. 5(b)]. The 2D map for a complete pyramid is characterized by a main lobe elongated along the perpendicular direction with a monotonic intensity decrease. For pyramidlike islands on a (001) surface, the main side facets are (111), in which case the angle between a side and bottom facet is 54.7°. Only this pyramid type will be consid-

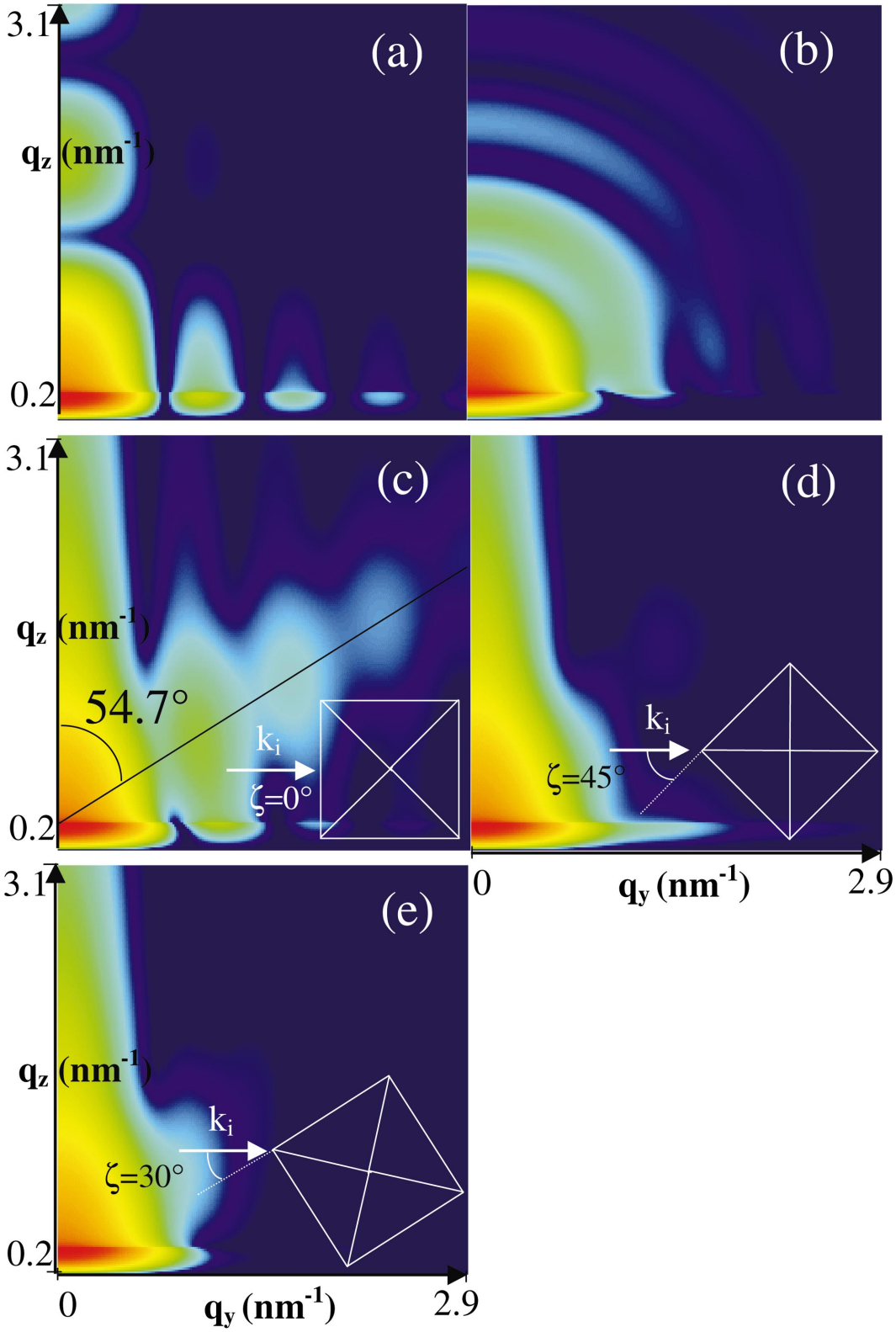

FIG. 5. (Color) The 2D $|F(\mathbf{q})|^2$ factor calculated within the DWBA of (a) a cylinder ($R=5$ nm and $H/R=1$), (b) a complete sphere ($R=5$ nm), (c) a complete pyramid with $R=5$ nm with the beam aligned along a face ($\zeta=0°$), (d) same as (c) but with the beam aligned along an edge ($\zeta=45°$), and (e) same as (c) but with $\zeta=30°$. The intensity is represented on a logarithmic scale. The same intensity scale is used for all these 2D patterns.

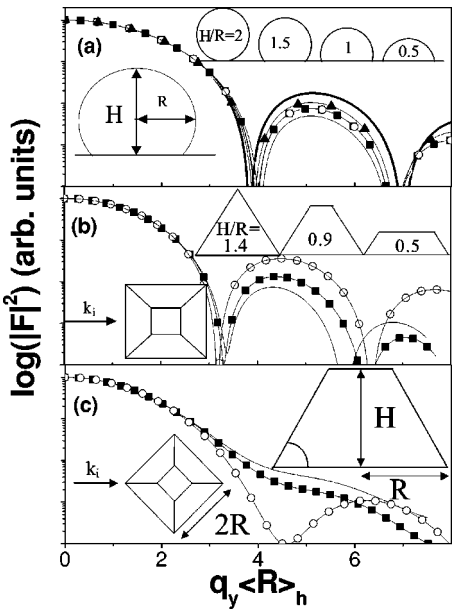

FIG. 6. Square modulus (logarithmic basis) of the form factor calculated within the BA at $q_x=q_z=0$ versus $q_y\langle R\rangle_h$. (a) Isotropic islands. Bold line, cylinder; filled triangles, sphere with $H/R=1.5$; open circles, $H/R=2$; filled squares, $H/R=1$; line, $H/R=0.5$. (b) Pyramid with the beam aligned along a face. Line, $H/R=1.4$; filled squares, $H/R=0.9$; open circles, $H/R=0.5$. (c) Same as (b) but with the beam aligned along an edge. $\langle R\rangle_h$ is the average of R over the island height.

ered in this paper. If the beam impinges on a face, pronounced scattering rods by facets appear at an angle of 54.7° with respect to the surface normal [cf. Fig. 5(c)]. When the angle ζ increases between 0 and 45°, these rods become less intense [cf. Figs. 5(d) and 5(e)]. Hence, we show that a simple qualitative inspection of a 2D GISAXS pattern may allow a first guess of the average island shape, e.g., symmetry and facets. However, this is not always possible, and a detailed analysis of the intensity evolution as a function of q_y and q_z is then necessary to provide additional information on the island shape.

3. Deducing island size and shape from a rapid data analysis

a. The small-polydispersity case. In the case of small polydispersity, i.e., islands close in size and shape, the positions of the form factor zeros are indicative of the morphological parameters. This is illustrated in Fig. 6 with the square modulus of the form factor as a function of $q_y\langle R\rangle_h$, where $\langle R\rangle_h$ is the average of R on the island height. For isotropic islands like cylinder and sphere based shapes, all the $|F(q_y\langle R\rangle_h)|^2$ functions are expressed with a Bessel function in the parallel plane and thus have their first zeros at $q_y\langle R\rangle_h\approx 3.9$, as shown in Fig. 6(a). For a pyramid based shape, for the beam aligned along a face, all the $|F(q_y\langle R\rangle_h)|^2$ functions are expressed with a $\sin(x)/x$ function and thus have their first zeros at $q_y\langle R\rangle_h\approx 3.3$, as shown in Fig. 6(b). For cylinder, sphere, and pyramid with the beam aligned along a face, the $|F(q_y\langle R\rangle_h)|^2$ function presents several well-pronounced lobes. For the beam along an edge, the first zero or minimum is at $q_y\langle R\rangle_h\approx 4.5$ for a heavily truncated pyramid (typically, $H/R\approx 0.5$) as shown in Fig. 6(c). This value corresponds to the previous zero value (beam aligned along a face) times the square root of 2. As a matter of fact, the measured distance in GISAXS is that perpendicular to $\mathbf{k}_i$. In contrast, the $|F(q_y\langle R\rangle_h)|^2$ function decreases in a monotonic way for a complete ($H/R=1.4$) or slightly truncated pyramid (typically, $H/R\approx 0.9$).

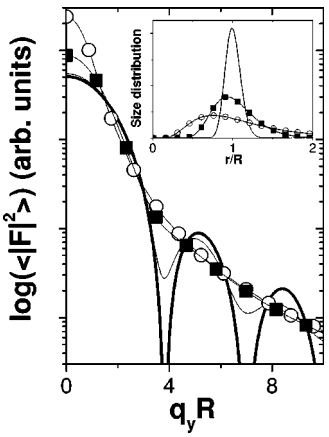

FIG. 7. The $\langle|F(q_yR)|^2\rangle$ function calculated within the BA for a cylinder at $q_x=q_z=0$, plotted (in a logarithmic basis) as a function of q_yR. Bold line, without any size distribution; thin line, with a log-normal distribution $\sigma=1.1$; filled squares, $\sigma=1.3$; open circles, $\sigma=1.7$. The inset shows the corresponding lateral size distributions.

b. The large-polydispersity case: Island size distribution. Island shape and size distribution is a natural consequence of the growth-coalescence process. The exact size distribution law is a central key in the numerous theoretical approaches to island growth.[24] Nevertheless, depending on the growth stage (nucleation, growth, or coalescence), the type of nucleation process (homogeneous or heterogeneous), the growth kinetics parameters (trapping energy, diffusion coefficient), the type of lattice mismatch relaxation, etc. it is difficult, if not impossible, to predict it. Usually, the observed lateral size distribution is well described by a log-normal probability distribution,

$$P_{\mathrm{LN}}(x)=\frac{1}{x\sqrt{2\pi}\ln(\sigma/X)}\exp\left\{-\frac{1}{2}\left[\frac{\ln(x/X)}{\ln(\sigma/X)}\right]^2\right\}, \quad (10)$$

where X is the central value and σ is linked to the full width at half maximum (FWHM). The asymmetry of this distribution is illustrated in the inset of Fig. 7 for various σ parameters. The obvious effect of the size distribution (cf. Fig. 7) is to smooth the scattering curve.

The height distribution and the cross correlation between lateral size and height distributions are also poorly known. From a practical point of view, we have chosen in the following analysis to fit them independently.

c. The large-polydispersity case: Asymptotic behavior of the form factor. In size distributed samples, further insight may be gained by studying the asymptotic behavior of the mean form factor, a limit which is currently named the Porod approach in the field of small-angle scattering in bulk

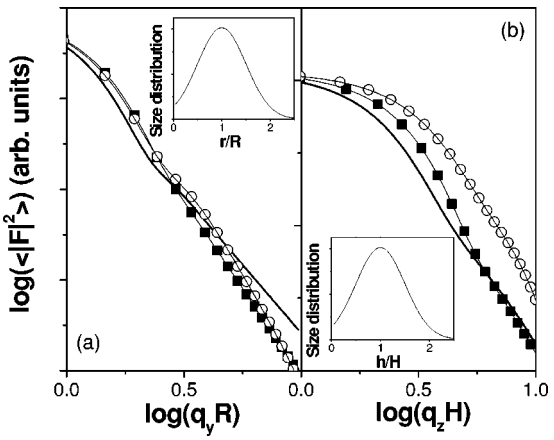

FIG. 8. Plots of $\log(\langle|F|^2\rangle)$ calculated within the BA (a) at the q_z position of total external reflection versus $\log(q_yR)$, and (b) at the q_y position of the interference maximum versus $\log(q_zH)$. Continuous line, cylinder with $R=1$ nm and $H/R=1$; filled squares, hemisphere with $R=1$ nm; open circles, pyramid with $R=1$ nm, $H/R=0.9$, and $\zeta=0°$. The insets of (a) and (b) show, respectively, the lateral and vertical log-normal size distributions of $\sigma=1.7$. Similar results are obtained within the DWBA.

samples. Whatever the approximation is, i.e., BA or DWBA, DA or LMA, the intensity at large q values is proportional to the average of the square modulus of the form factor. The curves $\ln(\langle|F|^2\rangle)$ versus $\ln(q_y)$ or $\ln(q_z)$ shown in Fig. 8 for simple geometrical shapes demonstrate that, for a sufficiently distributed sample, the intensity varies as q^{-n} with an exponent n that depends on the sharpness of the island. For instance, $n=3$ for a cylinder and 4 for a hemisphere or a pyramid ($H/R=0.9$, $\zeta=0°$) in the parallel direction, whereas $n=2.5$ for a cylinder and 3 for a hemisphere or a pyramid in the perpendicular direction in a range where $\ln(q_yR)$ or $\ln(q_zH)$ is comprised between 0.5 and 1. Hence, providing that measurements are performed sufficiently far away in reciprocal space (typically q_yR or $q_zH > 3.5\,\mathrm{nm}^{-1}$) with a high dynamics, each considered island shape is fully characterized by a set of slopes in both directions. It is also worth noticing that the difference from the 3D case, where $n=4$ for continuously curved interfaces, is due to the reduced dimensionality and the absence of the orientation average as supposed in the 3D Porod limit.[25]

D. Island interspacing and maximum of the interference function

In most of the literature,[2,3,7] the average interisland distance D is determined through the position of the GISAXS intensity maximum q_m by $D=2\pi/q_m$. However, as the GISAXS intensity is the product of the interference function $S(q_y)$ by the square modulus of the form factor, the GISAXS peak position q_m is shifted from the $S(q_y)$ peak position denoted q_p according to the form factor slope. This behavior is illustrated in Fig. 4 within the typical context of our Pd/MgO(001) studies for cylindrical islands of mean radius $\langle R\rangle=7.5$ nm. The interference function is obtained through the FT of the island pair correlation function extracted from TEM plane views (see Sec. III B 2 below). First, the GISAXS intensity maximum is located at $q_m\langle R\rangle=2.20$, corresponding to a distance of $2\pi/q_m=21.5$ nm, whereas the maximum of the interference function is at $q_p\langle R\rangle=2.92$ corresponding to a distance of $2\pi/q_p=16.2$ nm. There is a large discrepancy between these two distance determinations. Nevertheless, the distance determination from the interference function by $2\pi/q_p$ is not exact, as the exact mean interisland distance from the TEM analysis is $D=18.0$ nm. In the case of the azimuthal average of the paracrystalline domain,[12] the exact mean interisland distance is between the two roughly estimated distances. As a consequence, in order to get a precise determination of the mean interisland distance, it is extremely important to fit the experimental scattered intensity with an adequate model for the interference function.

III. EXPERIMENTS

A. Experimental procedure

1. GISAXS experiments

The GISAXS experiments were performed at the European Synchrotron Radiation Facility (ESRF) on the ID32 undulator beamline,[26] delivering a monochromatic, doubly focused x-ray beam. A dedicated experimental setup was built in order to perform GISAXS *in situ*, in UHV, during MBE, without any window before the sample, thus avoiding background scattering.[8] The beam size and divergence at the sample location were $0.05\times0.2\,\mathrm{mm}^2$ ($H\times V$) and 2×10^{-5} rad (H) and 4×10^{-6} rad (V) FWHM, respectively, with a flux at sample of approximately 10^{13} photons/s and an energy bandwidth of 2×10^{-4}.

The UHV chamber, mounted on a diffractometer, had a base pressure of 10^{-10} mbar. The beam entered the UHV chamber by a bellows hooked to the beamline, allowing for a small rotation of the chamber around the vertical axis, thus defining the angle of incidence of the x-ray beam with respect to the (vertical) sample surface. At the opposite side, a long cone was connected to an exit pipe through a CF38 bellows, and terminated by a 100 mm diameter beryllium window placed in front of the 2D detector, thus avoiding small-angle scattering background.

The scattering from the islands was collected on a 16-bit x-ray charge-coupled device detector (1242×1152 pixels for horizontal and vertical directions with a pixel size of $67\times67\,\mu\mathrm{m}^2$) that could be placed at a variable distance (between 900 and 1500 mm) from the sample. A motorized tungsten beamstop with a T shape was positioned perpendicularly to the sample surface in order to mask the transmitted and specularly reflected beams, because several orders of magnitude in intensity separate the diffuse scattering from the reflected beam. With this setup, the outgoing θ_f and α_f angles vary between 0 and approximately 3°. In reciprocal space, the momentum transfers q_y and q_z vary up to 2.6 (2.8) nm^{-1} for q_y (q_z) and up to 10 (14) for q_yR (q_zH). The q_x coordinate always remains negligible.

The data have been corrected for the flat field and the dark counts and the reference signal from the bare substrate prior to deposition has been substracted.

TABLE I. GISAXS results from best fits for Pd/MgO(001) deposited at different temeperatures T and with various thicknesses ε. The parameter q_m is the q value corresponding to the maximum of GISAXS intensity. The parameters D and D_{TEM} are the interisland distances obtained by GISAXS and TEM, respectively. The parameter R obtained by GISAXS is the radius for a sphere-based island and the maximum half lateral size for an octahedron with a square base, $\langle R\rangle$ is the average of R over the lateral size distribution, whereas $\langle H\rangle$ is the average of H over the vertical size distribution. The TEM radius R_{TEM} is that of a disk of equivalent surface. A log-normal distribution is used with a parameter σ (σ_R for the lateral size distribution and σ_H for the vertical one).

T (K)	ϵ (nm)	$2\pi/q_m$ (nm)	D (nm)	D_{TEM} (nm)	$\langle R\rangle$ (nm)	R_{TEM} (nm)	σ_R	$\sigma_{R\ \mathrm{TEM}}$	$\langle H\rangle$ (nm)	σ_H
550	0.9	6.4	6.17 ± 0.06	7.9 ± 1	1.66 ± 0.05	2.0 ± 0.4	1.3 ± 0.05	1.3 ± 0.1	2.06 ± 0.03	1.05 ± 0.05
650	0.1	17.1	16.22 ± 0.2		1.43 ± 0.05		1.15 ± 0.05		1.78 ± 0.02	1.1 ± 0.05
650	1.0	19.0	16.02 ± 0.2		7.3 ± 0.2		1.24 ± 0.05		5.71 ± 0.1	
740	3.0	21.5	18.0 ± 0.2	18.0 ± 3	7.5 ± 0.2	7.5 ± 1	1.25 ± 0.05	1.3 ± 0.1	6.41 ± 0.1	1.1 ± 0.05

2. Sample preparation

The growth of Pd on MgO(001) was studied during two experiments at $\theta_i=0$ with two different wavelengths (0.1127 nm for the growth at 550 and 740 K, and 0.1210 nm for the growth at 650 K), and with the angle of incidence $\alpha_i=\alpha_c$ (0.20° and 0.22°, respectively, for $\lambda=0.1127$ and 0.1210 nm). A load-lock system was used to insert the sample into the chamber.

The ($15\times15\times0.5\ \mathrm{mm}^3$) MgO(001) substrates, provided oriented and polished by Earth Chemical (Japan), were first annealed in air at 1500 °C for 24 h, which yielded crystals of very high quality with micrometer-size large (001) terraces. The contaminants segregated at the surface were next removed in a remote UHV chamber by Ar^+ ion bombardment (10 μA current and 0.6 keV energy) at 1500 °C, thus yielding clean flat terraces while keeping the high crystallinity, and finally annealed at 900 °C for 20 min and cooled down under 10^{-4} torr of O_2 in order to restore a perfect surface stoichiometry. The resulting stoichiometric MgO surfaces of very low roughness, with large terraces, i.e., a very small defect density, and high crystalline quality have been characterized elsewhere.[27] This procedure used to prepare the MgO(001) substrate results in extremely flat surfaces with a rms surface roughness of typically $\sigma\approx0.24$ nm.[27] These surfaces were protected by an approximately 1000 Å thick Ag film before being transferred in the x-ray chamber, where the Ag film was desorbed by annealing at approximately 700 °C. The deposition procedure for Pd was very close to that described in Ref. 27. Pd was evaporated at a rate of 1 Å/min using an Omicron EFM4 *e*-beam bombardment deposition cell with a 2 mm diameter, high purity (99.99%) rod. The flux was calibrated in situ by a quartz microbalance.

The MgO(001) substrates were stuck on a 1 mm thick Ta plate via a thin indium film. Heating was performed by a filament placed behind the Ta plate. The temperature of the MgO substrate was measured using an infrared pyrometer facing the Ta plate, and previously calibrated using the thermal expansion of the MgO lattice parameter as deduced from grazing incidence x-ray diffraction measurements.

3. TEM experiments

After the in situ GISAXS measurements during growth, the last deposits were analyzed by plane view TEM, with the carbon replica method. The samples were first encapsulated by an amorphous carbon layer a few tenths of a nanometer thick. The MgO substrate was next dissolved by a selective chemical attack in diluted HCl (15%). The carbon film containing the particles was then mounted on microscope grids. The grids were observed in a Jeol 2000 FX electron microscope operating at 200 kV, in transmission (bright field, dark field, and weak-beam dark field) and diffraction modes.

B. TEM and GISAXS analysis

Four samples with different thicknesses and prepared at different temperatures (0.9 nm at 550 K, 0.1 and 1 nm at 650 K, and 3.0 nm at 740 K) were studied with the two complementary techniques GISAXS and TEM. The main characteristics and results for these four samples are reported in Table I.

1. TEM analysis

The growth of Pd nanoislands on MgO(001) has been thoroughly investigated in the past as it represents a model catalyst of metallic islands on oxides.[28] The deposit morphology depends markedly on the preparation conditions and in particular on the temperature.

For the final (0.9 nm thick) deposit at 550 K [see Fig. 9(a)], most islands adopt the cube/cube [Pd(001)‖MgO(001)] epitaxial relationship with slight azimuth misorientations. A few particles have a [Pd(111)‖MgO(001)] epitaxial relationship. Some particles have already coalesced. The island density is approximately $(1.6\pm0.1)\times10^{12}\ \mathrm{cm}^{-2}$. The average radius of the noncoalesced islands is 1.5 nm and that of the coalesced islands is 2.5 nm. As shown in Fig. 9(a), only very few particles have a square outline. Most of them do not have a precise geometrical shape.

For the final (3.0 nm thick) deposit at 650 K [see Fig. 9(b)], the diffraction study indicates a very good (001) island epitaxy with better defined shapes (truncated pyramids for the smallest, octahedrons for the largest). The rectangular islands correspond to coalesced islands. There are a few triangular islands in (111) epitaxy.

For the final (3.0 nm thick) deposit at 740 K [see Fig. 9(c)], a predominantly (001) island epitaxy is found, with some (111) island orientation. The island density is not ho-

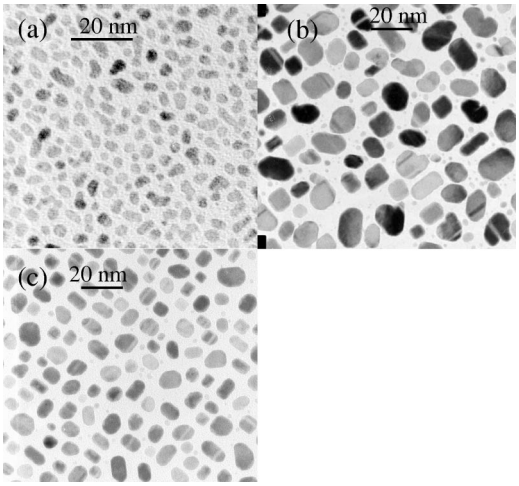

FIG. 9. TEM plane views after carbon replica of the Pd/MgO(001) samples in the final deposition state at (a) 550 K (0.9 nm thick Pd), (b) 650 K (3.0 nm thick Pd), and (c) 740 K (3.0 nm thick Pd).

mogeneous and is approximately $(3\pm1.2)\times10^{11}$ cm^{-2}. The average island radius is 4.5 nm and the islands are (111), (001), and (110) faceted. The height/radius ratio is 0.54 for islands with a square outline and varies between 0.8 and 1 for the other islands with rectangular, octahedral, and triangular outlines.

2. Interference function deduced from TEM

The GISAXS data were first fitted using different model interference functions.[12] However, none of them allowed us to satisfactorily reproduce the exact shape of the GISAXS data close to the origin of reciprocal space. We thus resorted to digitalized TEM plane views to define an ad hoc interference function. The island pair correlation function $g(r)$ was determined from the number of island centers of mass per unit of surface located at a distance between r and $r+dr$ from the original island. Care was taken to avoid image edge effects by excluding the borderline islands. Large-scale pictures with a few thousands of islands thus allowed to derive $g(r)$ and $S(q_{\|})$, the latter being fitted with a two-parameter function D,ω (D is the interisland distance and ω the disorder parameter) in order to introduce it in the fit procedure. The analytical expression for $S(q_{\|})$ is given in the Appendix. Ultimately, this function, determined on the final deposits, was found much more appropriate than the model functions to fit the GISAXS data for all deposits.

3. Analysis of GISAXS patterns

Qualitatively, the experimental GISAXS patterns present two large scattering lobes visible along the parallel direction, separated by the specular reflectivity, partly hidden by the beam stop. The extent of the intensity parallel (perpendicular) to the surface is inversely proportional to the average lateral size (height) of the island. The separation between the two main lobes is inversely proportional to the average separation between neighboring islands.

The GISAXS formalism described above has been used, within the DWBA and the LMA, to analyze the experimental data, unless otherwise mentioned. It has been checked that the GISAXS simulation was not affected by the low roughness of the MgO(001) substrate even at large **q**. Hence, the substrate roughness was neglected in the Fresnel reflectivity for the GISAXS calculation. Two cuts of the intensity in the (q_y,q_z) plane have been simultaneously fitted using a Levenberg-Marquadt χ^2 criterion minimization. One cut is parallel to the surface at the q_z position of maximum intensity and one is perpendicular to it at the q_y position of the interference maximum. Then a 2D GISAXS pattern is simulated with the parameters obtained from the previous fits. All the parameters obtained are gathered in Table I, together with those deduced from TEM. Several Pd/MgO(001) deposits were analyzed.

a. Pd/MgO(001) at 550 K. For the 0.9 nm thick Pd/MgO(001) deposit at 550 K, the 2D GISAXS experimental pattern with the corresponding analysis is displayed in Fig. 10. Owing to the TEM plane views and the GISAXS perpendicular asymptotic behavior corresponding to a straight line of slope -3 [see inset of Fig. 10(c)], the mean island has a sphere-based shape.

b. Pd/MgO(001) at 650 K. For the 0.1 nm thick Pd/MgO(001) deposit at 650 K, the GISAXS data and analysis are presented in Fig. 11. Since no TEM data were recorded for this deposit, the mean island shape used to fit the GISAXS, a truncated pyramid with a square base, was deduced from other microscopy work for similar temperature and island size conditions.[29] A very good agreement is obtained between the simulated and experimental data. Note the very small size distribution deduced from the fits (see Table I) for this small amount of deposited material.

For the 1 nm thick Pd/MgO(001) deposit at 650 K, Fig. 12 displays the 2D GISAXS experimental patterns and the corresponding analysis with the incident beam along the MgO[110] (MgO[100]) direction. The 2D GISAXS patterns present a scattering rod at 54.7° with respect to the surface normal in the ⟨110⟩ direction but not in the ⟨100⟩ direction. This indicates that palladium forms oriented faceted islands with {100} and {111} facets on the MgO(001) surface. Moreover, in the case of faceted islands, the second- and even sometimes third-order scattering peaks perpendicular to the surface are indicative of flat (001) terraces and of a narrow height distribution. All these features point to a truncated octahedronlike average shape as seen from TEM plane views. The simulated GISAXS patterns well reproduce the general features of the experimental GISAXS patterns, especially the scattering rod along the (111) direction visible in Fig. 12(a). As an example, one experimental GISAXS pattern (that with a scattering rod at 54.7° with respect to the surface normal in the ⟨110⟩ direction) has been simulated within the DA [see Fig. 12(g)]. Notice that neither the DWBA-LMA nor the DWBA-DA correctly reproduce the experimental diffuse scattering close to the beam stop.

c. Pd/MgO(001) at 740 K. For the 3.0 nm thick Pd depos-

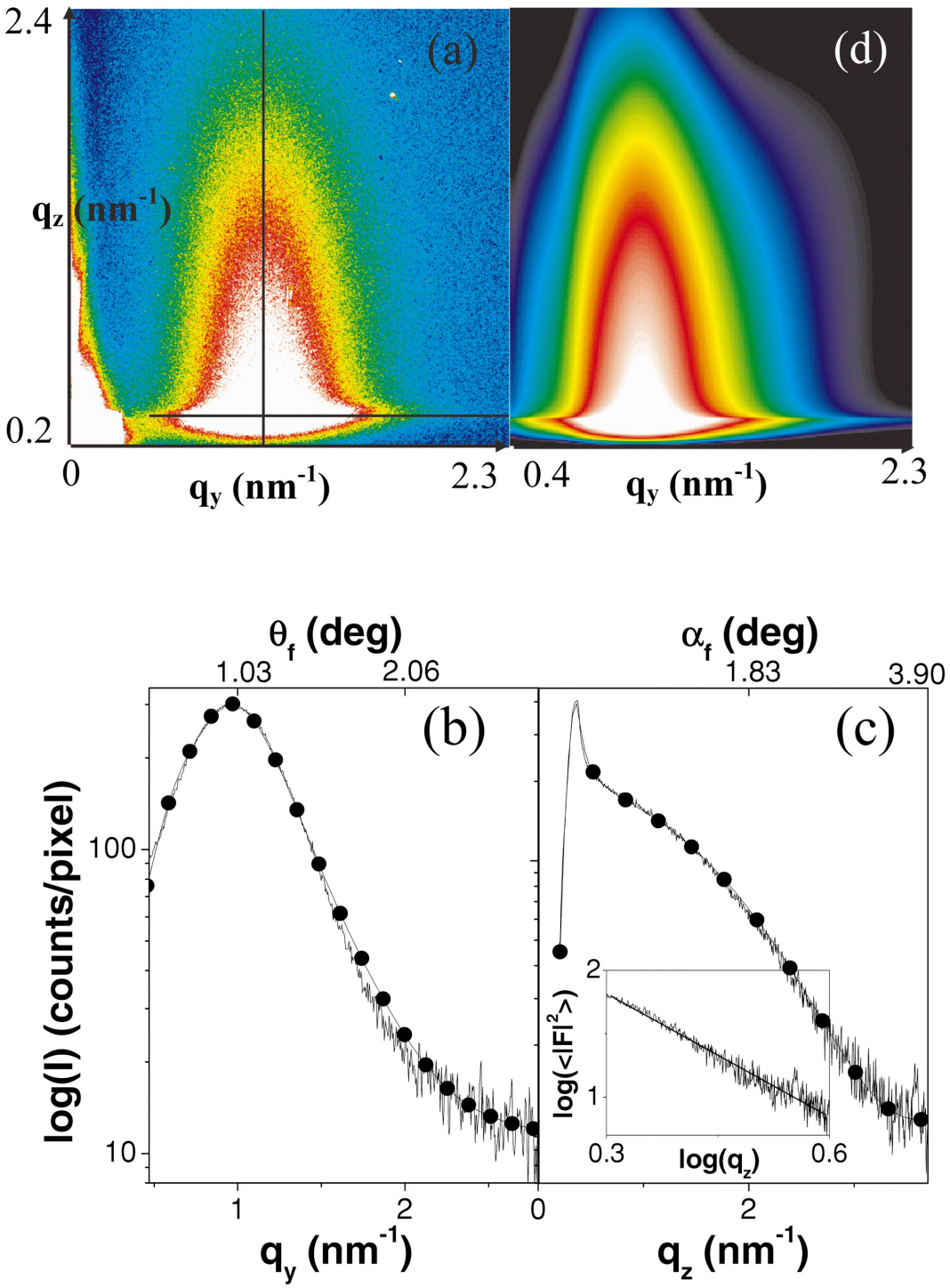

FIG. 10. (Color) 2D GISAXS intensity for a 0.9 nm thick Pd/MgO(001) deposit at 550 K. (a) Experimental 2D pattern with a spreading of the reflected beam. (b) Continuous line, cut of the experimental pattern parallel to the surface corresponding to the horizontal black line in (a); disks, best fit of the experimental cut. The intensity is in a logarithmic basis. (c) Same as (b) but cut perpendicular to the surface corresponding to the vertical black line in (a). The inset displays the asymptotic behavior of the experimental curve (c). (d) 2D lobe simulated with the parameters obtained from the parallel and perpendicular fits and reported in Table I. The intensity is represented on a logarithmic scale. The same intensity scale is used for both the experimental and simulated 2D patterns. This intensity scale corresponds to that used for the parallel and perpendicular cuts.

ited on a MgO(001) substrate at 740 K, the mean island shape is also assumed to be a truncated octahedron with a square base. Figure 13 shows the experimental GISAXS pattern and the corresponding analysis.

In all cases considered, the interisland distance obtained from the fit is slightly smaller than that obtained by the rough estimate $D=2\pi/q_m$ (see Table I), illustrating the issue of Sec. II D.

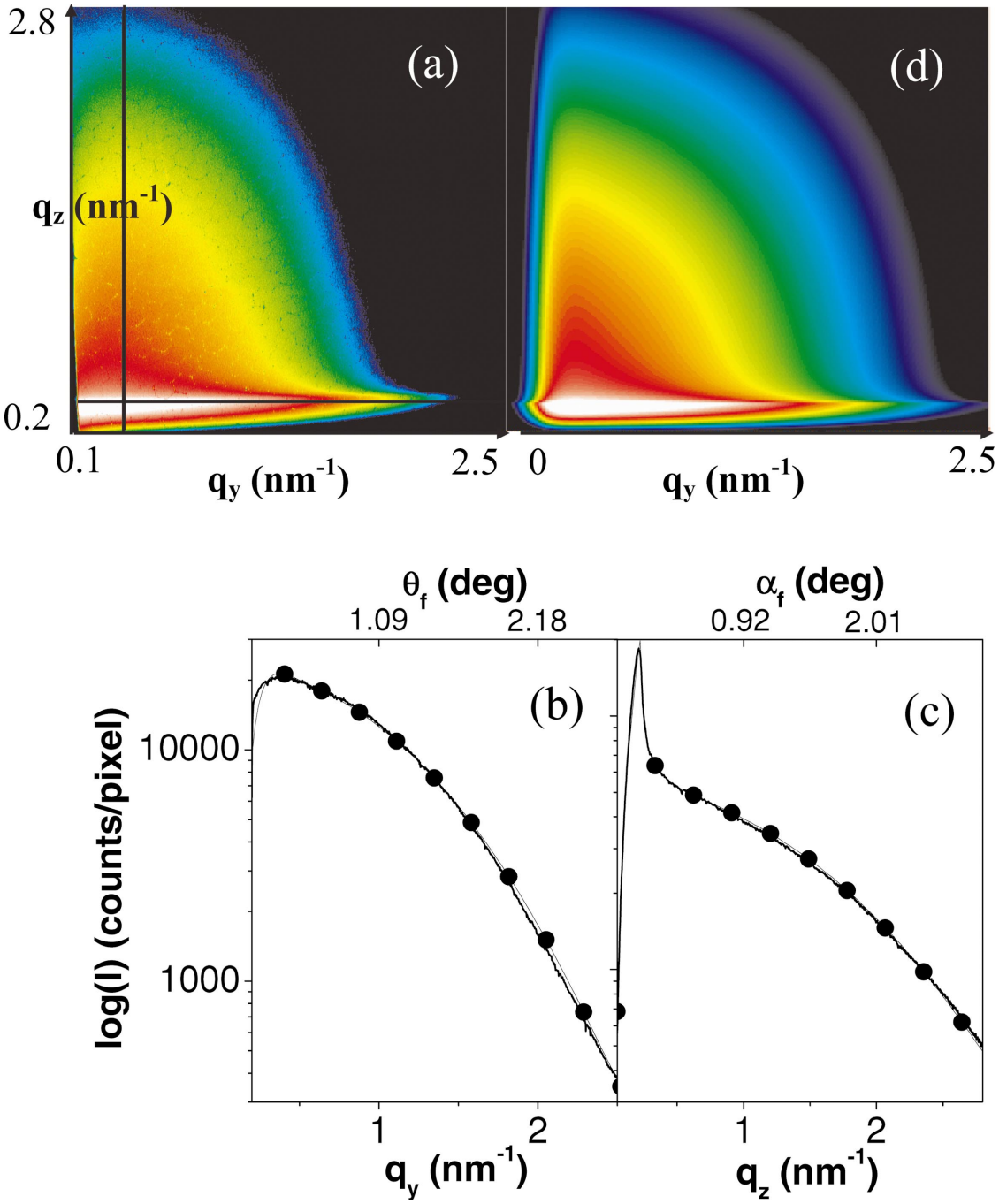

FIG. 11. (Color) 2D GISAXS intensity for a 0.1 nm thick Pd/MgO(001) deposit at 650 K. (a) Experimental pattern. (b) Continuous line, cut of the experimental pattern parallel to the surface corresponding to the horizontal black line in (a); disks, best fit of the experimental cut. The intensity is in a logarithmic basis. (c) Same as (b) but cut perpendicular to the surface corresponding to the vertical black line in (a). (d) 2D pattern simulated with the parameters obtained from the parallel and perpendicular fits and reported in Table I. The intensity is represented on a logarithmic scale. The same intensity scale is used for both the experimental and simulated 2D patterns. This intensity scale corresponds to that used for the parallel and perpendicular cuts.

IV. DISCUSSION

A. Comparison between GISAXS and TEM results

Let us compare the dimensional parameters deduced from GISAXS and from TEM for 0.9 nm thick Pd at 550 K and 3.0 nm thick Pd at 740 K. For the latter case, the agreement is excellent for all parameters, unambiguously demonstrating the adequacy of the GISAXS measurements and quantitative analysis. For the former case, the agreement is good as concerns the size distribution parameter σ_R. However, the interisland distance and radius deduced from GISAXS are approximately 20% smaller than those deduced from TEM. First of all, the TEM and GISAXS statistics are very different. As a matter of fact, TEM probes only a very small por-

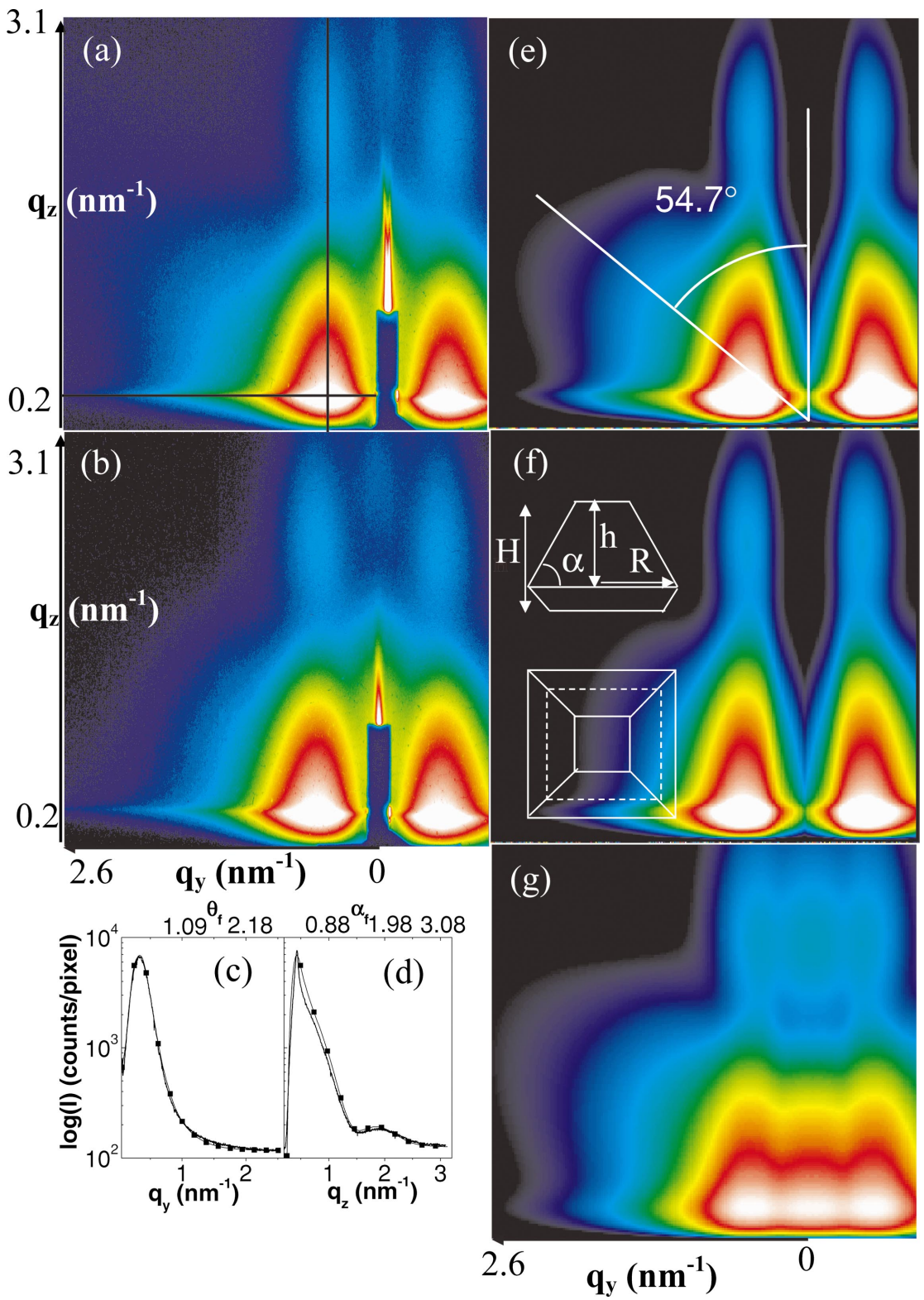

FIG. 12. (Color) 2D GISAXS intensity for a 1.0 nm thick Pd/MgO(001) deposit at 650 K. (a) Experimental patterns with the incident beam along the MgO[110] direction, and (b) same as (a) but with the incident beam along the MgO[100] direction. Black lines show the positions of the two cuts used to fit the data, parallel and perpendicular to the surface. For the sake of clarity, we show only (c) parallel and (d) perpendicular cuts for the 2D GISAXS pattern taken with the beam along the island edge (b). Continuous line, experimental cuts; filled squares, best fit of experimental cut. (e) and (f) Simulated 2D GISAXS patterns of (a) and (b), respectively, obtained after fitting the above experimental cuts and using an island shape of a truncated octahedron with a square base schematically drawn. (g) Same as (e) but within the DA. Note that the truncation rod visible in (a) and (b) has not been simulated in (e), (f), and (g). The intensity is represented on a logarithmic scale. The same intensity scale is used for both the experimental and simulated 2D patterns. This intensity scale corresponds to that used for the parallel and perpendicular cuts.

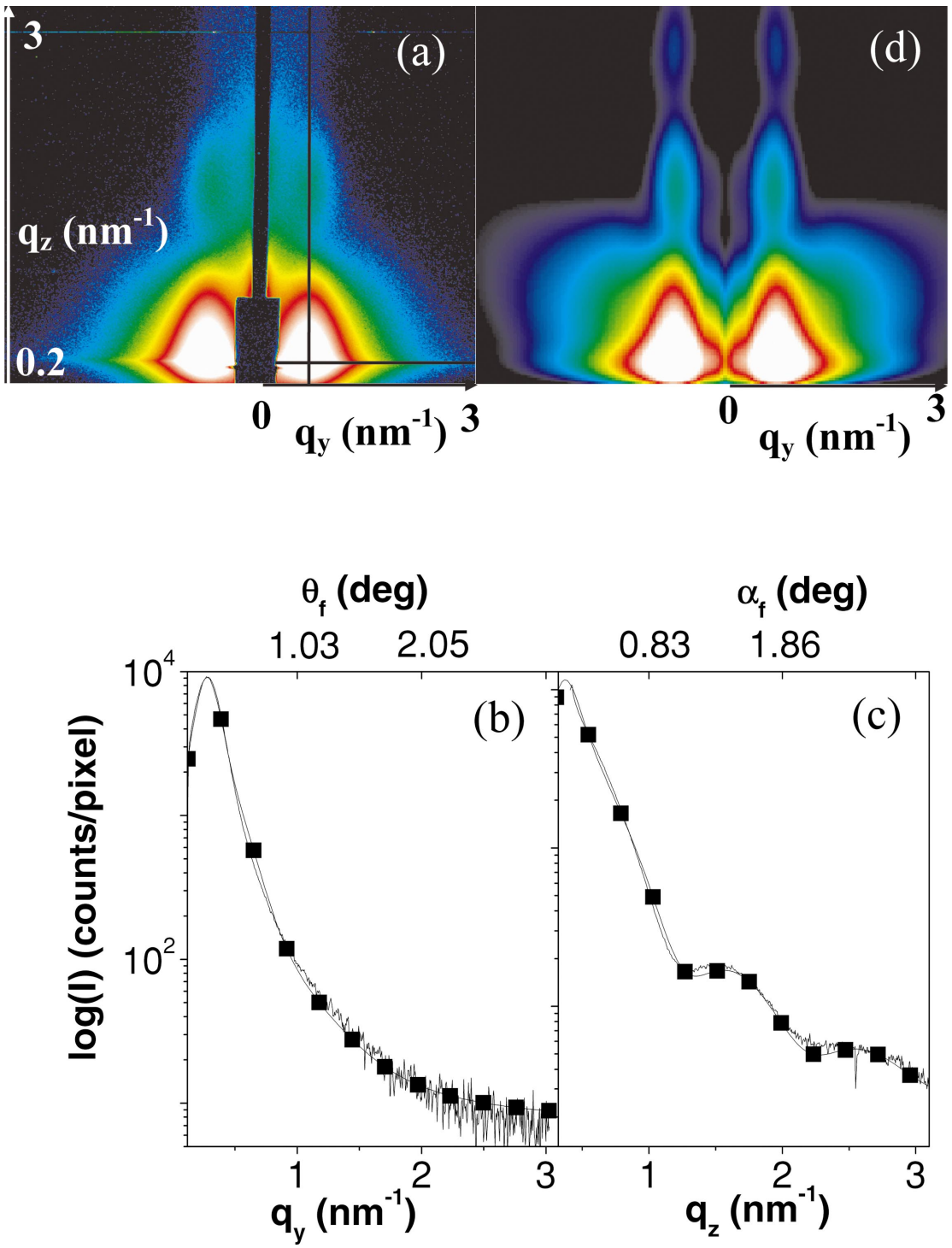

FIG. 13. (Color) (a) 2D GISAXS experimental intensity for a 3.0 nm thick Pd/MgO(001) deposit at 740 K. (a) Experimental pattern. (b) Continuous line, cut of the experimental pattern parallel to the surface corresponding to the horizontal black line in (a); filled squares, best fit of the experimental cut. (c) Same as (b) but cut perpendicular to the surface corresponding to the vertical black line in (a). (d) 2D pattern simulated with the parameters obtained from the parallel and perpendicular fits. Note that the truncation rod visible in (a) has not been simulated in (d). The intensity is represented on a logarithmic scale. The same intensity scale is used for both the experimental and simulated 2D patterns. This intensity scale corresponds to that used for the parallel and perpendicular cuts.

tion of the surface, as opposed to GISAXS. Hence, the observed difference in the TEM and GISAXS results might arise from inhomogeneity of the island distribution on the surface. Moreover, this difference is likely related to the very diverse and not always compact shapes of the particles for this low temperature deposit [see Fig. 9(a)]. Obviously, in this case, representing these diverse shapes by a simple spherical shape is a crude approximation.

B. Wulff's construction

Particularly interesting is the 650 K case, for which the interisland distance D first decreases between 0 and 0.3 nm deposited, next stays constant up to 1.5 nm, and finally increases. Since the island density is inversely proportional to D^2, the first stage corresponds to nucleation of islands (increasing density), the second to island growth (constant density), and the last to coalescence of neighboring islands. In addition, up to 1.5 nm deposited, the island aspect ratio $H/2R$ is found constant and equal to 0.6, as is the ratio $h/2R$ (equal to 0.45), where h is the top height of the octahedron. All these observations show that, for the 1 nm thick deposit, the islands have reached their equilibrium shape, which is thus a truncated octahedron with square base, since this is the only shape correctly fitting the experimental GISAXS pattern. At 650 K, the mobility of Pd atoms on MgO(001) and Pd clusters is very large, so that the islands reach their equilibrium shape on a subsecond time scale. The equilibrium state is thus reached before recording the GISAXS pattern. This truncated octahedron is actually a very good approximation to the truncated cubo-octahedron described in the literature.[9] This allows us to use the Wulff-Kaishew construction,[30,31] to deduce the interfacial energy β related to the aspect ratio as:

$$\beta = 2\sigma_{001}\left[1 - \frac{H}{2R} \times \frac{\sigma_{111}}{\eta_{001}} \times \frac{1}{\sin(\theta)}\right], \tag{11}$$

where $\sigma_{001} = 1.64$ J/m^2 ($\sigma_{111} = \sqrt{3/2}\sigma_{001}$) is the surface specific energy of the (001) [(111)] facet and $\theta = 54.7°$ is the angle between the (001) and (111) facets.[32,33] This yields $\beta \approx 1.1$ J/m^2, which compares well with the value of 0.947 J/m^2 deduced from contact angle measurements of a liquid Pd droplet on MgO(001) and to a recent experimental value[34,35] of 0.91 J/m^2. Thus under adequate conditions, GISAXS may give access, nondestructively, to the equilibrium shape of the islands.[35] This is no longer possible in the coalescence regime, in which the shape is not the equilibrium one, with a smaller aspect ratio. However, a recent kinetic Monte Carlo study of the growth-coalescence process associated with our morphological determination of growth will allow us to deduce the energetic barriers involved in the growth. In the coalescence regime, different cluster shapes are observed, including square and rectangular islands and some more complex profiles, as evidenced by the TEM plane view of the 3 nm thick deposit at 650 K in Fig. 9(b).

C. Height distribution

At the very beginning of growth, in the nucleation regime, the 0.1 nm thick Pd/MgO(001) deposit has small vertical and lateral size distributions, which are similar. Then, for a Pd deposit from a few 0.1 to several nanometers, a striking result is that the height distribution is smaller than the lateral size distribution whatever the temperature is from 550 to 740 K (see Table I). This behavior, which seems to be independent of temperature and film thickness, is believed to originate from growth mechanisms. First, the denser (111) facets grow faster than the (001) facets. Second, while the (111) side facets grow from both vapor phase and atom diffusion, the (001) top facets grow mostly from the vapor phase as if they were isolated, because of the high energy barrier an atom has to overcome to jump from a (111) to a (001) facet.[36,37]

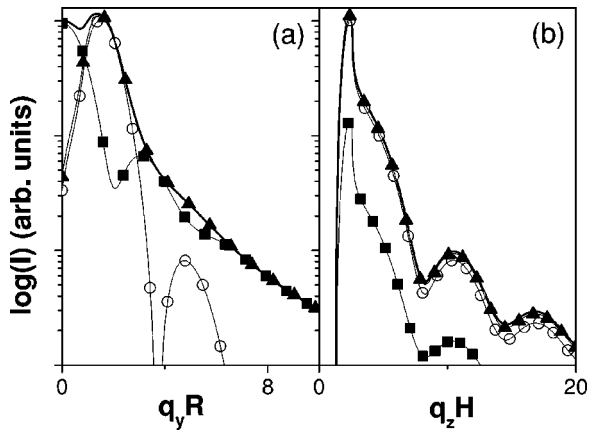

FIG. 14. (a) Intensity versus q_yR for a cylinder within the DWBA. Open circles, $I_1 = S(q_yR) \times \langle |F(q_yR)| \rangle^2$; filled squares, $I_2 = \langle |F(q_yR)|^2 \rangle - \langle |F(q_yR)| \rangle^2$; bold line, $I_1 + I_2$, i.e., the GISAXS intensity within the DA; triangles, GISAXS intensity within the LMA. (b) Same as (a) but versus q_zH. The parallel (perpendicular) direction is taken at the maximum intensity in the perpendicular (parallel) direction. The numerical values used for the simulation are those of 0.9 nm Pd/MgO(001) at 550 K.

D. Diffuse scattering

1. Evidence of diffuse scattering in GISAXS

Let us compare the DA and LMA results (see Fig. 14). In the DA, in the parallel direction, incoherent scattering dominates over coherent scattering for small ($q_yR < 1$) and large ($q_yR > 3$) q values. Close to the position of the interference function maximum ($q_yR \approx 1.5$), the situation is reversed and $\Phi_0(q_yR)$ is equal to only 10% of $S(q_yR) \times \langle |F(q_yR)| \rangle^2$. In the LMA, this small-angle scattering is absent, which points to the fact that in our experimental data a long-range size-position or size-size coupling exists. Notice that at high q values the two approximations give essentially the same results.

2. Size-position correlation deduced from TEM views

To gain further insight into possible island correlations, a more precise analysis was undertaken using the TEM plane views. The nearest neighbor (NN) diameter and interisland distance are shown versus the central island diameter for Pd/MgO(001) at 650 K in Fig. 15. Only a very weak correlation between the island sizes is obtained whatever the deposition temperature. This means that, on average, each island is surrounded by islands of different sizes accordingly to the overall size distribution. By contrast, a significant correlation between the island size and separation is deduced. The linear regression of the correlation between the island size and separation has a positive slope at the three temperatures studied, meaning that the larger the central island, the

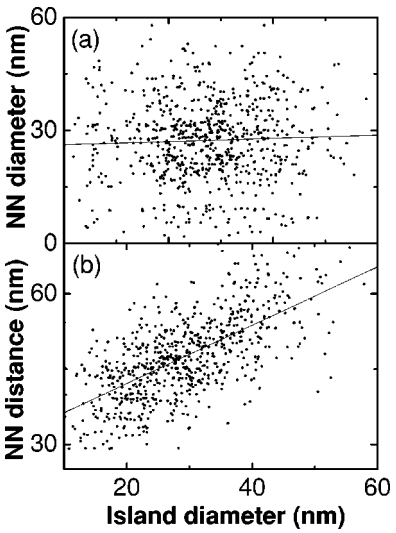

FIG. 15. (a) Correlation between the central island diameter and the diameter of its NNs for Pd/MgO(001) at 650 K. The slope of the linear regression is 0.043. For information, the slope of the linear regression is −0.008 at 550 K and 0.034 at 740 K. (b) Correlation between the central island diameter and the distance between NN islands for Pd at 650 K. The slope of the linear regression is 0.580. For information, the slope of the linear regression is 0.405 at 550 K and 0.351 at 740 K.

larger the distance from its NNs. This can be linked to the depletion zone of the islands. In the growth mode, the islands grow due to the diffusion of the atoms from the depletion zone, whose area is proportional to the island perimeter. Indeed, for submonolayer deposits, recent simulations suggested that the variation of capture rate with island size differs from mean field predictions, where the environment of each island is assumed independent of island size and shape.[38–42] Furthermore, in the coalescence regime, the zones often described as Voronoi cells merge.

3. Estimated GISAXS diffuse scattering

The influence of such correlations on the scattered intensity can be directly calculated as the positions and the sizes of the islands are known from TEM. From Eq. (2), the diffuse scattering is given by

$$I_d(\mathbf{q}) = \sum_m \Phi_m(\mathbf{q}) \times e^{-i\mathbf{q}\cdot\mathbf{r_m}}. \tag{12}$$

By approximating each island scattering power by that of a disk of equivalent surface, it is possible to evaluate the sum $I_d(\mathbf{q})$ up to a fixed distance cutoff (see Fig. 16). The scattering $I_{d0}(\mathbf{q})$ corresponds to $\Phi_0(\mathbf{q})$, $I_{d1}(\mathbf{q})$ is the diffuse scattering obtained by considering the NN shell around each island, and $I_{d2}(\mathbf{q})$ is the diffuse scattering obtained up to the second NN shell. For a larger cutoff, the curves obtained are noisy due to poor statistics and thus are not represented here. For Pd/MgO(001) at 550 K [see Fig. 16(a)], the incoherent diffuse scattering intensity is nearly independent of the size of the neighbor shell used for the calculation. On the contrary, for the deposition at 650 [see Fig. 16(b)] and 740 K [see Fig. 16(c)], the $I_{d3}(q_y)$ peak is larger and narrower than the $I_{d0}(q_y)$ one at small q_yR. This example shows that a high order correlation between scattering objects can strongly influence the diffuse scattering, particularly close to the origin of the reciprocal space in the parallel direction, and reduce the intensity as compared to that expected in the DA. In short, the best approximation for analyzing data is the LMA, even though with this model the island-island correlations are overestimated.

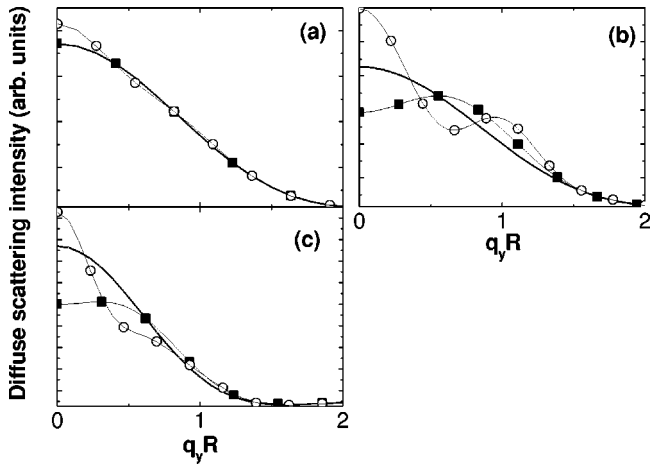

FIG. 16. Diffuse scattering calculated with a cylinder shape versus q_yR for Pd at (a) 550 K (0.9 nm thick Pd), (b) 650 K (3.0 nm thick Pd), and (c) 740 K (3.0 nm thick Pd) deduced from the TEM plane views. Continuous line, I_{d0}; filled squares, I_{d1}; open circles, I_{d2}.

V. CONCLUSION

In this article, we have shown that the DWBA formalism for islands on a substrate is mandatory for correct analysis of GISAXS data. In almost all previous studies, the LMA has been implicitly assumed, in which neighboring islands are supposed to have identical sizes. Within this approximation, the distribution of island size does not yield any incoherent scattering. The simulation of our GISAXS data within the LMA demonstrates the existence of incoherent diffuse scattering at small q_y along q_z, but the other extreme approximation, the DA, assuming complete size-size and size-separation decorrelation yields a too large diffuse scattering. This indicates that some correlation between the islands is present. A detailed analysis of TEM plane views of some deposits has shown at least a strong size-separation correlation. This evidence of the failure of the LMA and DA was possible because of the negligible background and the high dynamics of intensity variations, which allowed us to measure the weak incoherent scattering. Going beyond such approximations would imply the difficult task of modeling the island partial pair correlation functions, i.e., the pair correlation functions according to the size of the islands. Nevertheless, the LMA and DA allow us to reproduce the experimental intensity at large q_y values, where the diffuse scattering becomes negligible and where both models converge, and allow us to deduce the width of the size distributions with

accuracy in excellent agreement with that determined by the TEM.

In these concentrated systems, at small angles, the GISAXS data strongly depend both on the form factor and on the interference function. This latter cannot be extracted from the data for disordered systems like the present ones, and have thus to be modeled. Hence, an ad hoc pair correlation function, determined by fitting the pair correlation function evaluated from TEM data, has been used for the fits.

Finally, the 2D GISAXS patterns of four Pd/MgO(001) deposits (0.9 nm at 550 K, 0.1 and 1.0 nm at 650 K, and 3.0 nm at 740 K) have been quantitatively analyzed, and the dimensional parameters deduced. For two of them, these parameters have been compared to those obtained from TEM and an excellent agreement is found. Moreover, a striking feature of these analyses is the much smaller spread of the island height as compared to the island lateral extension, due to the nucleation-growth-coalescence process.

ACKNOWLEDGMENT

We would like to thank all the staff of the ESRF ID32 beamline for their invaluable help during the mounting of the GISAXS setup and the measurements. SP2M is a laboratory associated with the Université Joseph Fourier, Grenoble, France.

APPENDIX

The TEM derived $S(q_{\parallel})$ function has been fitted with the following analytical expression:

$$S(q_{\parallel}) = S_1(q_{\parallel}) + \omega \times e^{-A_1 q_{\parallel} D/\pi} \times \cos(A_2 \times D \times q_{\parallel}) \times \left(1 - \frac{1}{1 + e^{A_3 D(q_{\parallel} - A_4 \pi/D)}}\right)$$

with

$$S_1(q_{\parallel}) = 1 - \frac{1}{1 + e^{A_5 D(q_{\parallel} - A_6 \pi/D)}}.$$

The parameter D is the interisland distance and ω is the disorder parameter. For the 0.9 nm thick Pd/MgO(001) deposit at 550 K, the following numerical values have been obtained: $A_1 = 1.43$, $A_2 = 0.84$, $A_3 = 1.33$, $A_4 = 1.5$, $A_5 = 1.7$, and $A_6 = 1.13$.

[1] J. R. Levine, J. B. Cohen, Y. W. Chung, and P. Georgopoulos, J. Appl. Crystallogr. **22**, 528 (1989).
[2] J. R. Levine, J. B. Cohen, and Y. W. Chung, Surf. Sci. **248**, 215 (1991).
[3] A. Naudon and D. Thiaudière, J. Appl. Crystallogr. **30**, 822 (1997).
[4] D. Thiaudière, O. Proux, J.-S. Micha, C. Revenant, J.-R. Regnard, and S. Lequien, Physica B **283**, 114 (2000).
[5] F. Gonella, E. Cattaruzza, G. Battaglin, F. D'Acapito, C. Sada, P. Mazzoldi, C. Maurizio, G. Mattei, A. Martorama, A. Longo, and F. Zontone, J. Non-Cryst. Solids **280**, 241 (2001).
[6] T. Roch, V. Holy, A. Daniel, E. Höflinger, M. Meduna, T. H. Metzger, G. Bauer, J. Zhu, K. Brunner, and G. Abstreiter, J. Phys. D **34**, A6 (2001).
[7] M. Schmidbauer, Th. Wiebach, H. Raidt, M. Hanke, R. Köhler, and H. Wawra, J. Phys. D **32**, A230 (1999).
[8] G. Renaud, R. Lazzari, C. Revenant, A. Barbier, M. Noblet, O. Ulrich, F. Leroy, J. Jupille, Y. Borensztein, C. R. Henry, J.-P. Deville, F. Scheurer, J. Mane-Mane, and O. Fruchart, Science **300**, 1416 (2003).
[9] C. R. Henry, Surf. Sci. Rep. **31**, 235 (1998).
[10] G. Renaud, Surf. Sci. Rep. **32**, 1 (1998).
[11] O. Fruchart, G. Renaud, J.-P. Deville, A. Barbier, F. Scheurer, M. Klaua, J. Barthel, M. Noblet, O. Ulrich, J. Mané-Mané, and J. Kirschner, J. Cryst. Growth **237-239**, 2035 (2002).
[12] R. Lazzari, J. Appl. Crystallogr. **35**, 406 (2002).
[13] A. Guinier and G. Fournet, *Small Angle Scattering of X-rays* (Wiley, New York, 1955).
[14] G. Porod, in *Small Angle X-ray Scattering*, edited by O. Glatter and O. Kratky (Academic, New York, 1982), p. 37.
[15] R. Hosemann and S. N. Bagchi, *Direct Analysis of Diffraction by Matter* (North-Holland, Amsterdam, 1962).
[16] A. Guinier, *X-Ray Diffraction in Crystals, Imperfect Crystals, and Amorphous Bodies* (Dover, New York, 1963).
[17] J. S. Pedersen, J. Appl. Crystallogr. **27**, 595 (1994).
[18] J. S. Pedersen, P. Vysckocil, B. Schönfeld, and G. Kostorz, J. Appl. Crystallogr. **30**, 975 (1997).
[19] A. Naudon, in *Modern Aspects of Small-Angle Scattering*, edited by H. Brumberger (Kluwer Academic, The Netherlands, 1995), p. 181.
[20] G. H. Vineyard, Phys. Rev. B **26**, 4146 (1982).
[21] S. K. Sinha, E. B. Sirota, S. Garoff, and H. B. Stanley, Phys. Rev. B **38**, 2297 (1988).
[22] M. Rauscher, R. Paniago, H. Metzger, Z. Kovats, J. Domke, J. Peisl, H.-D. Pfannes, J. Schulze, and I. Eisele, J. Appl. Phys. **86**, 6763 (1999).
[23] J. Als-Nielsen and D. McMorrow, *Elements of Modern X-ray Physics* (Wiley, New York, 2001), p. 88.
[24] J. A. Venables, *Introduction to Surface and Thin Film Processes* (Cambridge University Press, Cambridge, England, 2000).
[25] O. Robach, Ph.D. thesis, University of Grenoble I, 1997.
[26] http://www.esrf.fr
[27] O. Robach, G. Renaud, and A. Barbier, Surf. Sci. **401**, 227 (1998).
[28] G. Renaud, A. Barbier, and O. Robach, Phys. Rev. B **60**, 5872 (1999).
[29] C. R. Henry, C. Chapon, C. Duriez, and S. Giorgio, Surf. Sci. **253**, 177 (1991).
[30] G. Wulff, Z. Kristallogr. **34**, 449 (1901).
[31] R. Kaishew, Thesis, University of Dresden, 1952, p. 81.
[32] C. L. Liu, J. M. Cohen, J. B. Adams, and A. F. Voter, Surf. Sci. **253**, 334 (1991).
[33] A. C. Shi, Phys. Rev. B **36**, 9068 (1987).
[34] A. F. Moodie and C. E. Marble, Philos. Mag. **35**, 201 (1977).

[35] H. Graoui, S. Giorgio, and C. R. Henry, Surf. Sci. **417**, 350 (1998).
[36] G. Ehrlich and F. G. Hudda, J. Chem. Phys. **44**, 1030 (1966).
[37] R. L. Schwoebel and E. J. Shipsey, J. Appl. Phys. **37**, 3682 (1966).
[38] J. G. Amar, M. N. Popescu, and F. Family, Phys. Rev. Lett. **86**, 3092 (2001).
[39] M. C. Bartelt, C. R. Stoldt, C. J. Jenks, P. A. Thiel, and J. W. Evans, Phys. Rev. B **59**, 3125 (1999).
[40] M. C. Bartelt, A. K. Schmid, J. W. Evans, and R. Q. Hwang, Phys. Rev. Lett. **81**, 1901 (1998).
[41] M. C. Bartelt and J. W. Evans, Phys. Rev. B **54**, R17 359 (1996).
[42] L. Bardotti, C. R. Stoldt, C. J. Jenks, M. C. Bartelt, J. W. Evans, and P. A. Thiel, Phys. Rev. B **57**, 12 544 (1998).